https://doi.org/10.5194/egusphere-2025-1884
Preprint. Discussion started: 10 June 2025

Characterizing Nearshore Icebergs in front of the Dalk Glacier, East Antarctica by UAV Observation

Mingyue Nong[1,2], Xuying Liu[3], Teng Li[1,2], Baogang Zhang[4,5], Qi Liang[1,2], Lei Zheng[1,2], Tiancheng Zhao[6,7], and Xiao Cheng[1,2]

[1]School of Geospatial Engineering and Science, Sun Yat-sen University, Southern Marine Science and Engineering Guangdong Laboratory (Zhuhai), Zhuhai 519082, China
[2]Key Laboratory of Comprehensive Observation of Polar Environment (Sun Yat-sen University), Ministry of Education, Zhuhai 519082, China
[3]Institute of Artificial Intelligence, Shaoxing University, Shaoxing 312000, China
[4]Faculty of Geographical Sciences, Beijing Normal University, Beijing 100875, China
[5]State Key Laboratory of Remote Sensing and Digital Earth, Beijing Normal University, Beijing 100875, China
[6]School of Environmental Science, Nanjing Xiaozhuang University, Nanjing 211171, China
[7]School of Geography, Nanjing Normal University, Nanjing 210023, China

Correspondence: Teng Li (liteng28@mail.sysu.edu.cn)

Abstract. Icebergs are the products of glacier calving, and they float on the ocean, influencing ocean circulation and maritime activities. Extensive research has been carried out on the distribution and shapes of icebergs. However, current research mainly focuses on medium and large icebergs. Smaller icebergs, though numerous, are less studied due to the difficulty of detecting them in satellite imagery. In our research, high-resolution images obtained by an Unmanned Aerial Vehicle (UAV) during the Chinese 36th Antarctic expedition were used for the study of smaller icebergs. We extracted nearshore icebergs in front of Dalk Glacier using a method combining superpixel segmentation and Random Forest classification. We directly calculated the area and freeboard of these icebergs by combining Digital Surface Model (DSM) and further calculated their volume. Our research found that DSM generated without control points exhibit a dome effect, and fitting with a surface effectively mitigates this error. Our research identified 187 icebergs, whose area follows a power law distribution with a slope of -1.13. The area/volume relationships obtained from the UAV survey align surprisingly well with existing iceberg parameterization in large-scale ocean models, which was firstly proved to also be valid in growler and berg bit scale by observation evidence. Our research provides new data and insights into the distribution and geometry of small icebergs. Our research reveals the capability of UAVs in extracting iceberg geometric features, highlighting their advantages and discussing the potential and challenges of using UAVs in polar iceberg research.

1 Introduction

Iceberg calving, the process of ice detachment from glacier termini or ice shelf margins, releases icebergs into the surrounding marine environment (Alley et al., 2023; Benn et al., 2007). These calved icebergs exhibit substantial differences in size and morphology, exerting multifaceted impacts on the surrounding environment. Freshwater-laden icebergs alter local and

https://doi.org/10.5194/egusphere-2025-1884
Preprint. Discussion started: 10 June 2025

basin-scale marine biogeochemistry through modifications of carbon, trace element, and nutrient concentrations (Duprat et al., 2016; Ingels et al., 2021), thereby reshaping marine ecosystems. On the other hand, icebergs also influence human activities. Iceberg capsizing and calving-induced water-surface oscillations pose threats to coastal infrastructure (Ke et al., 2022), while the drifting trajectories of icebergs obstruct navigation and increase maritime risks (Bigg et al., 2018). Consequently, systematic quantification of spatiotemporal iceberg distributions, coupled with dimensional analyses of area, freeboard, and volume (Dammann et al., 2019; Stern et al., 2016), is imperative for both regional environment impact assessments and the development or validation of iceberg-resolving ocean circulation models.

Since the 1970s, researchers have conducted surveys and tracking of medium to large icebergs in the Southern Ocean. In 1978, the U.S. National Ice Center (NIC) began using visible light, synthetic aperture radar (SAR), and near-infrared imagery to continuously track Antarctic icebergs with a long axis exceeding 18 km (www.natice.noaa.gov). Building upon this foundation, Brigham Young University's Microwave Earth Remote Sensing (MERS) Laboratory initiated analysis in 1999, integrating microwave scatterometer data with NIC records to track icebergs longer than 5 km, and established a unified trajectory database (Budge and Long, 2018; Stuart and Long, 2011). Extensive research efforts have systematically recorded ice shelf-originated megabergs, notably encompassing the 1,580 km^2 D28 iceberg calved from Amery Ice Shelf (Liu et al., 2022; Li et al., 2020a) the 4,320 km^2 A76 iceberg calved from Ronne Ice Shelf (Moctezuma-Flores et al., 2023), and the tabular icebergs C28A and C28B, which originated from the C28 iceberg calved from the Mertz Ice Tongue (Li et al., 2018). Tournadre et al. (2016) integrated data from nine altimeters from 1992 to 2014, estimating iceberg size distributions within the range of 0.1-10,000 km^2 and revealing the power law of their area. With the development of machine learning, Barbat et al. (2019) achieves sub-kilometer detection using Radarsat-1/2 imagery via superpixel segmentation and ensemble learning, systematically mapping icebergs larger than 0.1 km^2 and exploring regional distribution patterns. Despite these advances, existing studies exhibit critical observational gaps: coastal iceberg inventories remain disproportionately focused on medium and large icebergs, neglecting the ubiquitous yet under-sampled population of smaller icebergs.

Quantitative analysis of fjord-hosted iceberg distributions enables investigation of their spatiotemporal dynamics, providing critical insights into glacial calving regimes and iceberg area decrease pathways. Notably, Scheick et al. (2019) established a methodological framework combining semi-automated Landsat delineation with time-series comparisons of iceberg coverage indices, small-berg densities, and power law scaling in Disko Bay, revealing the change of glacier calving mechanics. Leveraging multi-resolution optical data (Landsat and PlanetLab), Rezvanbehbahani et al. (2020) compared different iceberg extraction methods and explored how icebergs change their shape. These studies focus on Greenland's enclosed fjords that are still less affected by ocean currents, while similar fine-scale researches are lacking for Antarctic glaciers.

The quantitative analysis of iceberg shape characteristics, especially how geometric parameters like length, width, area, freeboard, and volume relate to each other, is an important aspect of iceberg research. Hotzel and Miller (1983) established a dimensional scaling relationship through regression analyses of 1973-1978 Labrador Sea icebergs sampled during offshore drilling operations, revealing mean width-to-length ratios of 0.8:1 with extreme length-height ratios spanning 0.5:1 to 50:1. Subsequently, Orheim (1980) systematically characterized Antarctic icebergs employing Norwegian Antarctic Expedition datasets containing georeferenced parameters (length, width, freeboard, thickness), identifying a statistically constrained mean length-

https://doi.org/10.5194/egusphere-2025-1884
Preprint. Discussion started: 10 June 2025

width ratio of 1.5:1 across 24 iceberg specimens. Methodological limitations persist in iceberg size estimation using historical shipborne datasets, as navigational avoidance strategies inherently induce systematic under sampling. This route-dependent bias severely constrains spatially representativeness across oceanic scales. The research of Sulak et al. (2017) in three Greenland fjords found that iceberg area and volume exhibited an evident logarithmic relationship. At present, the calculation of iceberg volume and freshwater flux is mainly based on a series of basic assumptions such as iceberg shape and length-to-width ratio (Dammann et al., 2019; Sulak et al., 2017). And the accuracy of these assumptions remains difficult to validate through field observations. These studies about the effects of icebergs on the ocean focus on modeling iceberg trajectories and melting processes (Gladstone et al., 2001; Stern et al., 2016). However, given the abundance of small icebergs, whether these data accurately represent reality remains uncertain. To improve freshwater flux calculations, direct measurements and refined modeling of small iceberg geometries at meter-level scales are essential. However, due to limitations in data resolution, modeling these complex relationships remains challenging.

In recent years, Unmanned Aerial Vehicles (UAVs) have become operational tools in Antarctic observations, demonstrating sub-meter spatial resolution and adaptive survey strategies that significantly enhance glacier surface deformation monitoring precision (Li et al., 2020b). Equipped with multispectral sensors and real-time telemetry systems, UAVs enable dynamic tracking of iceberg trajectories while optimizing flight paths through continuous ice condition feedback (Carlson et al., 2019; Jones and Gudmundsson, 2015), providing technical support for acquiring high-resolution iceberg morphological data. The high-resolution UAV-based data can achieve a DSM precision of about 1 m and an iceberg freeboard precision of about 1.4 m, thus providing accurate validation data for satellite altimetry retrieval algorithms of icebergs (Guan et al., 2021). By conducting multiple UAV flights around the iceberg, high-resolution 3D iceberg models can be created after image processing (Carlson et al., 2019). High-resolution UAV-based topographic products allow simultaneous extraction of crevasse length and depth parameters (Qiao et al., 2023), effectively resolving spatiotemporal registration challenges in multi-source remote sensing data. LiDAR-equipped UAVs excels at capturing intricate details in complex environments, sensitives to fine morphological variations such as characterize an ice doline's interannual change on a centimeter scale (Li et al., 2020b). Integration with Autonomous Underwater Vehicles (AUVs), UAVs enable mapping of sea ice topography (Fan et al., 2023; Wadhams and Krogh, 2019). Schild et al. (2021) constructed three-dimensional iceberg geometry from UAVs and subsurface sonar data, and directly calculated the power law between iceberg area and volume from these two types of data. The similarity of their results to those of prior studies (Sulak et al., 2017) suggests that even without data from the bottom of the iceberg, high-precision UAVs data allow us to capture a credible total volume (Schild et al., 2021). This provides a basis for our iceberg research based on high-precision UAV data.

This research analyzes centimeter-scale UAV imagery captured over Dalk Glacier during Chinese 36th Antarctic Research Expedition. Employing superpixel segmentation and random forest algorithms, we systematically classify six surface types: sea ice, icebergs, sea water, melt ponds, shadow and rock, from which icebergs are subsequently extracted. Leveraging UAV-derived products with centimeter-scale resolution, we perform direct geometric measurements of iceberg areas and freeboard. Icebergs are categorized based on equivalent length and freeboard, and are then subjected to quantitative analyses, including an analysis of their quantity, spatial distribution, and the power law characteristics of their area. Additionally, our research explores

https://doi.org/10.5194/egusphere-2025-1884
Preprint. Discussion started: 10 June 2025

the area/volume relationship of small icebergs, comparing the results with data used in current iceberg parameterization in large-scale ocean models. Finally, our research concludes with a critical evaluation of UAV capabilities and limitations in advancing iceberg research, particularly regarding observational scalability and model-data integration challenges.

2 Study Area and Data

2.1 Study Area

Dalk Glacier is located on the east side of the Larsemann Hills in East Antarctica, about 3 km from both Zhongshan and Progress stations (Fig. 1(a)). It stretches approximately 15 km in length, with a front width of about 4 km, and flows northward into Dalkoybukta Bay (Skrypitsyna et al., 2023; Li et al., 2020b). The front of the glacier grows or calves periodically. At the beginning of 2019, the glacier calved and retreated about 400 m (Chen et al., 2020; Mishra et al., 2024; Qiao et al., 2023). The calving released a dense flux of icebergs into the front sea area. Research indicates these icebergs underwent shape change under combined wave and thermal erosion, posing tsunami risks to adjacent research infrastructure (Guan et al., 2021; Ke et al., 2022). According to the Landsat 8 imagery acquired on December 12, 2019, shown in Fig. 1(b), a large number of differently shaped and sized icebergs gathered in the nearshore zone of the Dalk Glacier. However, due to the low resolution of Landsat 8 imagery, accurately identifying these small icebergs remains challenging, making it impossible to precisely analyze their geometric features such as freeboard, area, length, and volume.

2.2 Data Collection

In our research, we collected UAV images captured by the polar remote sensing teams from Beijing Normal University and Sun Yat-Sen University during the Chinese 36th Antarctic expedition. At approximately 11:15 p.m. local time on December 17, 2019, the research team conducted a UAV survey mission over Dalk Glacier nearby Zhongshan Station.

The mission utilized the F200 UAV developed by Feima Robotics Laboratory. It is a fixed-wing fully automatic UAS, with a fuselage length of 1.07 m, a wingspan of 1.9 m, and a weight of 3.7 kg. It is capable of withstanding wind forces up to level 6, operates at altitudes ranging from 150 m to 1500 m, adapts to diverse environmental conditions, and supports GPS-PPK (Post-Processing Kinematic) technology. The reliability of this system has been validated through multiple previous Antarctic expeditions (Li et al., 2020b). The UAV was equipped with a Sony DSC-RX1RII full-frame camera with a 35 mm focal length, ensuring high-resolution image acquisition.

The flight mission consisted of three sorties, covering the area from the surface melt ponds near the southern grounding line to the front of Dalk Glacier. Ultimately, the research team completed an aerial survey of approximately 38 km^2, with a total flight distance of about 187 km, capturing 993 images. For follow-up analysis, 119 images from the first sortie were selected. The images were captured between 13:17 and 13:30 local time on December 17, 2019, at a flight altitude of approximately 925 m. The flight achieved an 81% forward overlap and a 70% side overlap, meeting the requirements for generating Digital Orthophoto Map (DOM) and Digital Surface Model (DSM) (Li et al., 2019).

https://doi.org/10.5194/egusphere-2025-1884
Preprint. Discussion started: 10 June 2025

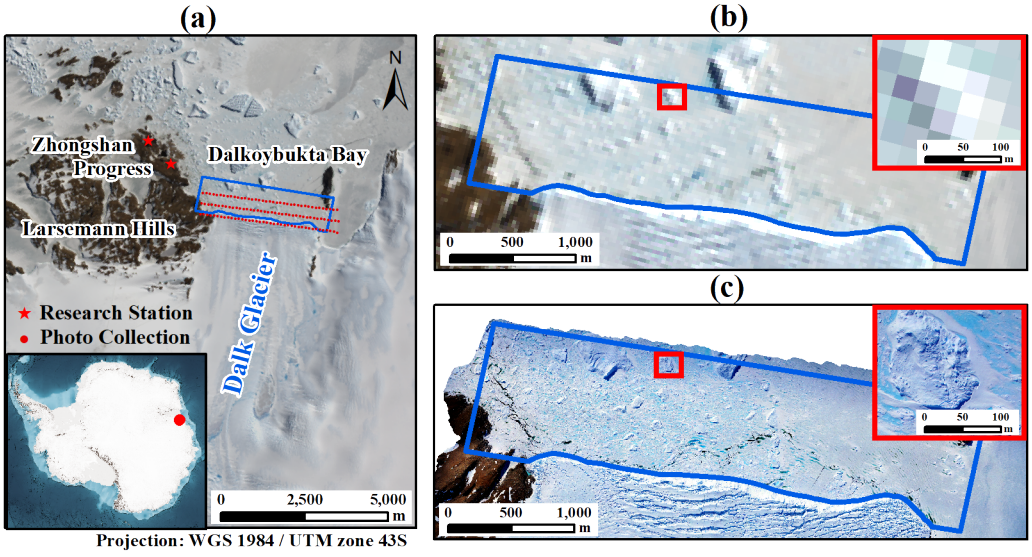

Figure 1. The study area. (a) Dalk Glacier's location, shown on the pansharpened 15 m resolution Landsat 8 true-color composite image acquired on December 12, 2019. The blue box outlines the nearshore icebergs for the following study, with red dots representing the camera positions. (b) Landsat 8 image of the study area with a 30 m resolution, acquired on December 12, 2019. (c) UAV image of the study area with a 0.2 m resolution, acquired on December 17, 2019. Taking the iceberg marked by the red box as an example, compared with the Landsat 8 image (b), the Detailed features of the iceberg can be observed more clearly in high-resolution UAV image (c).

3 Methods

The research method of this study consists of four main steps, as shown in Fig. 2. First, we generate the DOM and DSM using UAV imagery, and then conduct post-processing. Next, based on the DOM and DSM data, we use superpixel segmentation and random forest classification to classify the surface types and extract the icebergs. Finally, we extract the geometric features of the icebergs for subsequent analysis.

3.1 Photogrammetric Processing

We processed the data in Agisoft Metashape (version 2.1; https://www.agisoft.com), importing photos and POS data, and performing photo stitching using Structure from Motion (SfM) techniques, including photo alignment, point cloud generation, mesh reconstruction, and texture mapping. We ultimately obtained the DOM with a 0.2 m resolution and the DSM, generated using the WGS 84/UTM Zone 43S (EPSG : 32743) projection. The UAV-derived DOM clearly reveals extensive fast ice, surface melt ponds, and irregularly shaped icebergs distributed at the glacier front. A zoom-in section is shown in Fig. 1(c), where a comparison with pansharpened Landsat 8 imagery (Fig. 1(b)) demonstrates the UAV's capability to capture iceberg edge contours and surface textures with significantly higher detail and clarity.

https://doi.org/10.5194/egusphere-2025-1884
Preprint. Discussion started: 10 June 2025

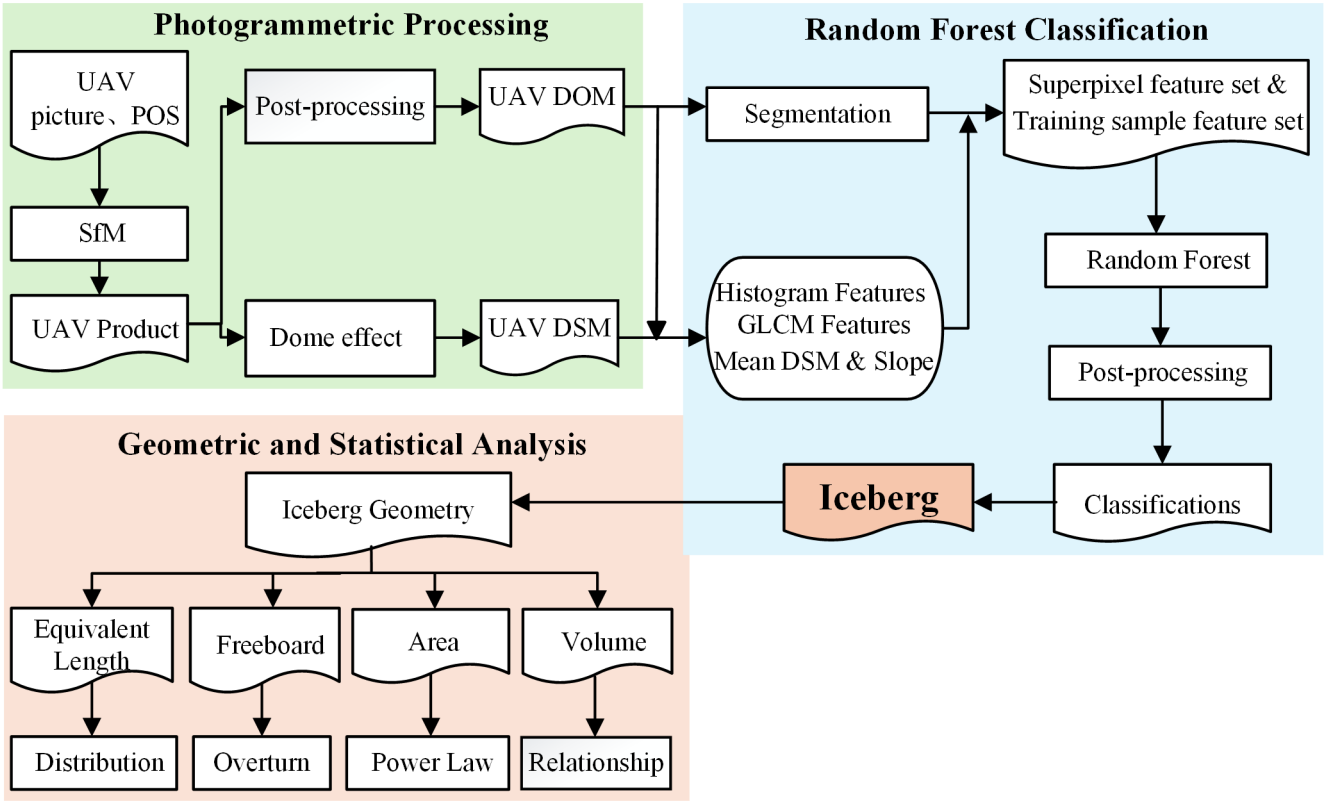

Figure 2. The workflow of this study includes three main parts: Photogrammetric Processing, Random Forest Classification, Geometric and Statistical Analysis. First, photogrammetric processing and some preprocessing steps are applied to the UAV images to generate DOM and DSM. Based on these datasets, a combination of superpixel segmentation and the random forest is employed to classify surface features in the study area and extract icebergs. Finally, the distribution and geometric relationships of the icebergs are analyzed based on their geometric parameters.

3.2 Dome Effect Correction

Compared with traditional aerial photogrammetry technology, the Structure from Motion (SfM) method, based on UAV images, can generate DSMs more conveniently. However, this method may introduce errors in the generated DSMs, such as the "dome effect" (James and Robson, 2014). The "dome effect" refers to the systematic deformation of the terrain surface caused by SfM reconstruction during the data acquisition process. This may arise from factors such as near-parallel flight path pattern, inaccurate camera parameters, or insufficient ground control points (GCPs), which may reduce the accuracy of the DSM (Wackrow and Chandler, 2011; Yurtseven, 2019).

The UAV survey area of this research is located in the front of the glacier and the sea, which is covered by the landfast sea ice. The operating environment is hazardous, impossible to lay GCPs, which makes it difficult to verify the absolute accuracy

https://doi.org/10.5194/egusphere-2025-1884
Preprint. Discussion started: 10 June 2025

of the DSM. As shown in Fig. 3(a), the initial DSM reveals a significant elevation difference between the sea ice on the left and right sides. By selecting sample points on the sea ice (Fig. 3(b)), the largest elevation difference was found to be up to 7 m (Fig. 3(c)), indicating an evident dome effect. To accurately extract geometric attributes such as iceberg freeboard, it is necessary to first perform DSM correction to eliminate the dome effect error. We adapted the method proposed by Magri and Toldo (2017), using the ground points to fit the dome effect with a paraboloid surface, and then subtracting this paraboloid from the original DSM to generate an error-corrected DSM.

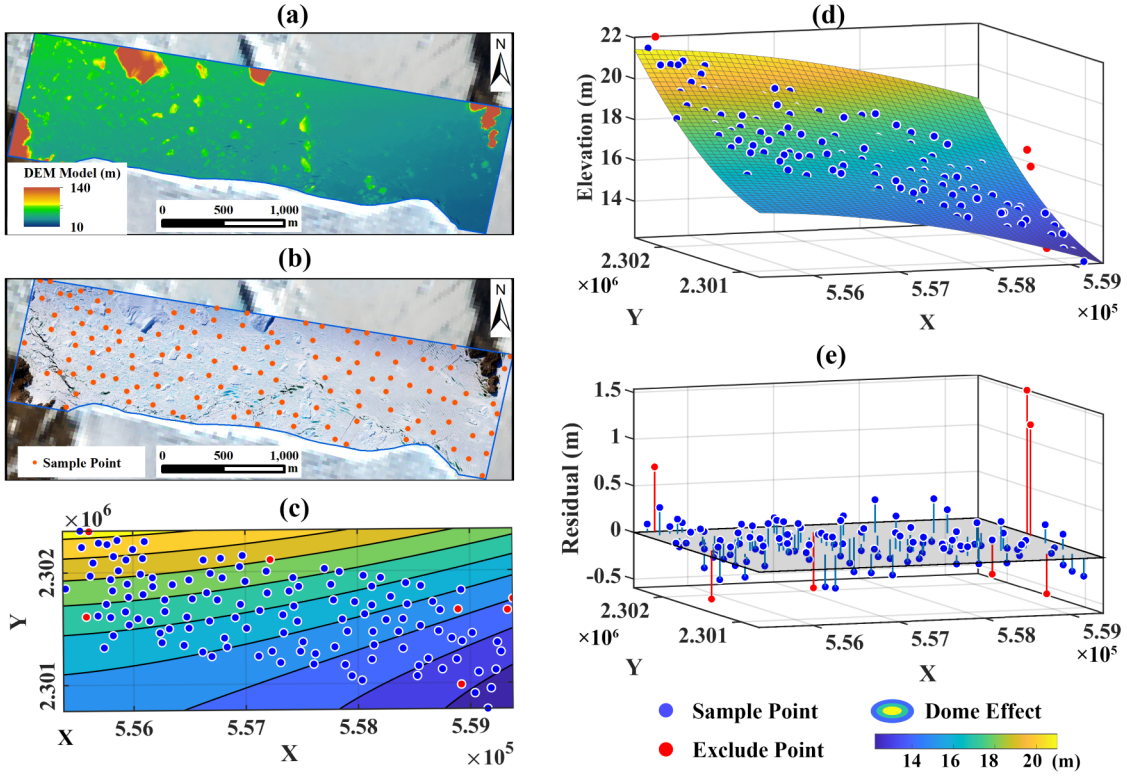

Figure 3. Recognition and correction of dome effect. (a) Initial DSM; (b) Distribution of sampling points in flat and stable sea ice surface; (c) Fitted dome effect contour plots; (d) Dome effect surface fitting diagram; (e) Deviation of the sampling points from the fitted surface.

Considering the data was collected in the austral summer, we assumed that the thickness of sea ice is relatively thin and uniform and that the ice surface was approximately at 0 m. We selected sample points in this area for paraboloid fitting. A quadratic polynomial was used for fitting the model (Equation 1):

$$f(x,y) = a_0 + a_1 x + a_2 y + a_3 x^2 + a_4 y^2 + a_5 xy \tag{1}$$

The 3D coordinates of each sample point, (x_i, y_i, z_i), are used to model the surface, and the fitting parameters a_i are calculated using the least squares method. After removing high-error sample points, the final fitting coefficients are obtained and

https://doi.org/10.5194/egusphere-2025-1884
Preprint. Discussion started: 10 June 2025

used to calculate the fitted elevation surface for the entire study area. Then, the fitted surface is subtracted from the original DSM to generate a DSM with the dome effect removed, which serves as the basis for subsequent analyses. Finally, profile line analysis is performed on both the original and corrected DSMs to assess the effectiveness of the dome effect error reduction method.

3.3 Random Forest Classification

While high-resolution UAV images provide details on the surface objects, they may also generate redundancy and interfere with the classification. In order to make full use of the advantages of high resolution of the image and improve the classification efficiency, the following steps are taken: firstly, the superpixel segmentation algorithm is used to divide the whole image into multiple superpixel units, and the superpixel is an object to be classified by the aggregation of the original pixels, which can retain the boundary information of the ground object, reduce the computational cost of pixel-level classification. Then, the features of each superpixel are extracted to construct the feature set of the object. Subsequently, the training samples were manually selected, and the random forest classifier was trained by using the machine learning method to classify and determine all superpixels. Finally, the final classification result was validated through visual inspection and correction.

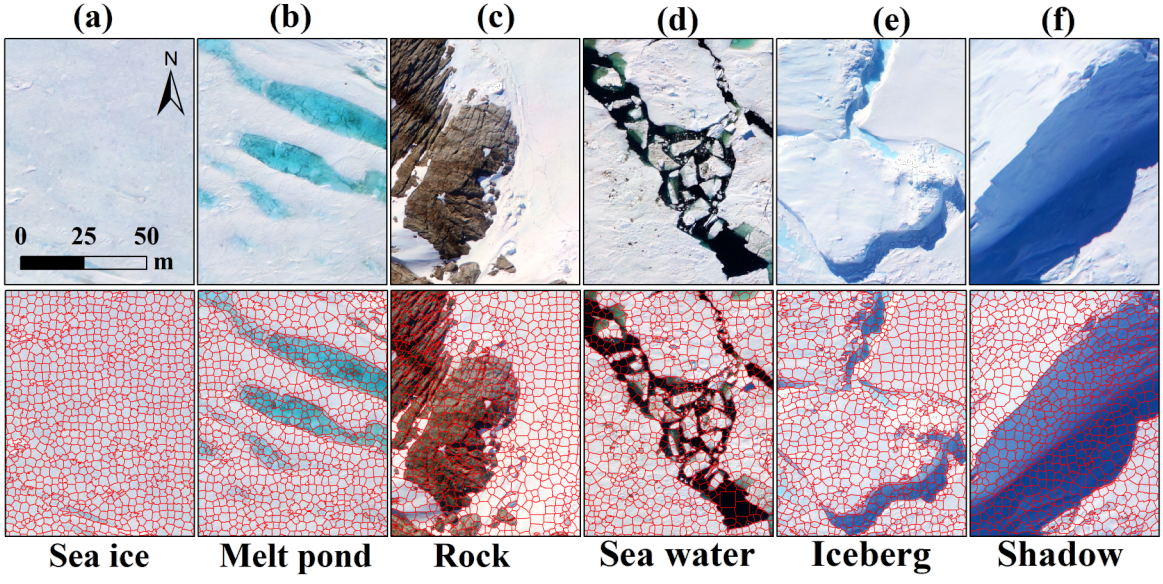

Figure 4. Surface and segmentations. (a) sea ice; (b) melt pond; (c) rock; (d) sea water; (e) iceberg; (f) shadow.

In our research, the Simple Linear Iterative Clustering (SLIC) algorithm (Achanta et al., 2012) is used for superpixel segmentation of DOM. The algorithm converts the color image into the CIELAB color space, combines the XY coordinates to generate 5-dimensional feature vectors, and then applies an improved K-means clustering algorithm to generate superpixels. Considering the slender shape of some features in the study area, an initial target of 500,000 superpixels was set, with the

https://doi.org/10.5194/egusphere-2025-1884
Preprint. Discussion started: 10 June 2025

compactness parameter set to 3 and the upper limit of the number of iterations set to 10. Finally, the DOM was divided into 421,252 superpixels, and the segmentation of the six types of surface are shown in Fig. 4.

After the image segmentation, six types of features are extracted from each superpixel to construct the feature set for classification. These features include histogram features (mean and standard deviation), texture features (entropy and contrast) derived from the GLCM, and topographic features (average elevation and average slope) derived from the DSM. For the six surface types, i.e. rock, iceberg, sea ice, melt pond, seawater, and shadow, 200 to 400 superpixels are manually selected to create a training sample set for the random forest classifier, which is then used to classify all superpixel objects.

After the classification, we convert the raster image into a vector layer and carry out visual inspection and correction. This includes merging small melt ponds on the iceberg into the iceberg objects, visually interpreting and redefining the shadow areas, and correcting misclassified sea ice and iceberg. During the analysis, we found that small icebergs with an area less than 30 m^2 are easily confused with ridges formed by sea ice compression, especially in areas close to the glacier front. Therefore, we focus on extracting and studying icebergs larger than 30 m^2.

3.4 Iceberg Geometric and Statistical Analysis

3.4.1 Iceberg geometry

In ArcMap, the geometric information of each iceberg is calculated. Based on the WGS 1984 / UTM Zone 43S projection, the area and perimeter of each iceberg on the waterline plane are calculated, and the equivalent length of the iceberg (the square root of the iceberg's area) is further derived.

Subsequently, combined with the DSM data, the elevation information of each iceberg's surface is extracted pixel-wise to determine the maximum freeboard of the iceberg, which serves as an indicator of the iceberg's local highest point. At the same time, the mean elevation of all pixels on the iceberg's surface is calculated as the freeboard, which will be used for subsequent volume and thickness estimations.

We use an iceberg density of 920 kg m^{-3} and a seawater density of 1025 kg m^{-3} based on previous study (Sulak et al., 2017), and calculate the total thickness and volume of the iceberg from the average freeboard and volume above the water, based on Archimedes' buoyancy principle.

3.4.2 Iceberg distribution

Based on the iceberg size classification method defined by the International Ice Patrol in Table 1 (Dammann et al., 2019), we classify the icebergs according to their freeboard and equivalent length. As two independent classification criteria, the size categories may differ for certain specific icebergs. We analyze the spatial distribution and quantity statistical distribution across different size scales.

According to the area of the obtained icebergs, we used the power law (Equation 2) to fit the occurrence of icebergs in varies areas.

$$P(x) \propto x^{-\alpha} \tag{2}$$

https://doi.org/10.5194/egusphere-2025-1884
Preprint. Discussion started: 10 June 2025

Table 1. Iceberg size classification defined by the International Ice Patrol

Size class	Height (m)	Length(m)
Growler	<1	<5
Bergy bit	<1-5	5-15
Small	5-15	15-60
Medium	15-45	60-122
Large	45-75	122-213
Very large	>75	>213

Where $P(x)$ is the probability density function (PDF) of the iceberg area, α is the power law exponent.

3.4.3 Area/volume relationships

Based on the iceberg data we extracted, and combined with the parameterization scheme widely used in ocean models, as shown in Table 2 (Gladstone et al., 2001; Stern et al., 2016), we fit the relationship between iceberg area and volume using the general power law. This allows us to explore and compare the area/volume relationships in both datasets.

$$V = aA^b \tag{3}$$

where V is the iceberg volume and A is the iceberg area, a and b representing the correlation coefficient.

In the ocean, icebergs may change shape due to melting, collisions, and other factors, leading to the potential for iceberg capsizing. This study performs an exploratory analysis of iceberg capsizing based on existing formulas (Equation 4), incorporating iceberg length and draft (Weeks and Mellor, 1978).

$$L < \sqrt{(0.92D^2 + 58.32)} \tag{4}$$

When the length of the iceberg L and the draft D meet the above formula, the iceberg tends to capsize.

4 Results

4.1 Dome Correction assessment

It has been demonstrated that direct georeferencing methods can generate high-precision UAV products without GCPs, even in harsh environments such as Antarctica (Tang et al., 2024). Based on the sample points, after continuous iterative optimization, the R^2 of the final fitting surface is 0.998, and the RMSE is 0.149 m. On this basis, the DSM of the entire study area was fitted, and the fitting surface was subtracted from the original DSM, to generate a DSM after dome correction (Fig. 5(a)).

https://doi.org/10.5194/egusphere-2025-1884
Preprint. Discussion started: 10 June 2025

Table 2. iceberg data from parameterization schemes used in ocean models.

Class	Mass (kg)	Length (m)	Area (km^2)	Thickness (m)	Scaling
Class 1	8.8×10^7	62	0.0026	40	2000
Class 2	4.1×10^8	104	0.0072	67	200
Class 3	3.3×10^9	209	0.0290	133	50
Class 4	1.8×10^{10}	426	0.1200	175	20
Class 5	3.8×10^{10}	518	0.1800	250	10
Class 6	7.5×10^{10}	728	0.3500	250	5
Class 7	1.2×10^{11}	920	0.5600	250	2
Class 8	2.2×10^{11}	1246	1.0000	250	1
Class 9	3.9×10^{11}	1659	1.8000	250	1
Class 10	7.4×10^{11}	2285	3.5000	250	1

In order to verify the correction effect, three cross-sectional lines in different directions were selected to generate profile lines. The results show that the sea area at the front of the glacier is mainly covered by landfast sea ice. And most of the area is low and flat, except for the high elevation of icebergs and sea ice ridges. The line after dome correction tends to be horizontal in the low-value area, and the elevation of the landfast sea ice part is close to the 0 m reference line, indicating the good fitting correction, and provides more accurate and reliable DSM support for subsequent research.

4.2 Classifications results

Using superpixel segmentation combined with the random forest classifier, the overall classification accuracy reaches 0.927 (Table 3). Compared with traditional pixel-based classification methods, this method significantly improves classification accuracy while maintaining the integrity of surface objects.

Melt ponds, seawater, rock, and shadows showed better classification performance, with fewer misclassifications and errors. However, icebergs and sea ice exhibited more severe confusion due to their similar reflectance and complex shapes. Icebergs and sea ice appear quite similar in RGB channels. And icebergs with unusual shapes may present large freeboard variations, while some sea ice ridges show high elevation, making it difficult to distinguish. Therefore, manual correction is required to extract icebergs accurately.

Icebergs of varying shapes and sizes are distributed across the sea ice surfaces in the front sea area, with numerous melt ponds found on both sea ice and icebergs (Fig. 6). The ice leads are mainly concentrated on the left side of the image, which

https://doi.org/10.5194/egusphere-2025-1884
Preprint. Discussion started: 10 June 2025

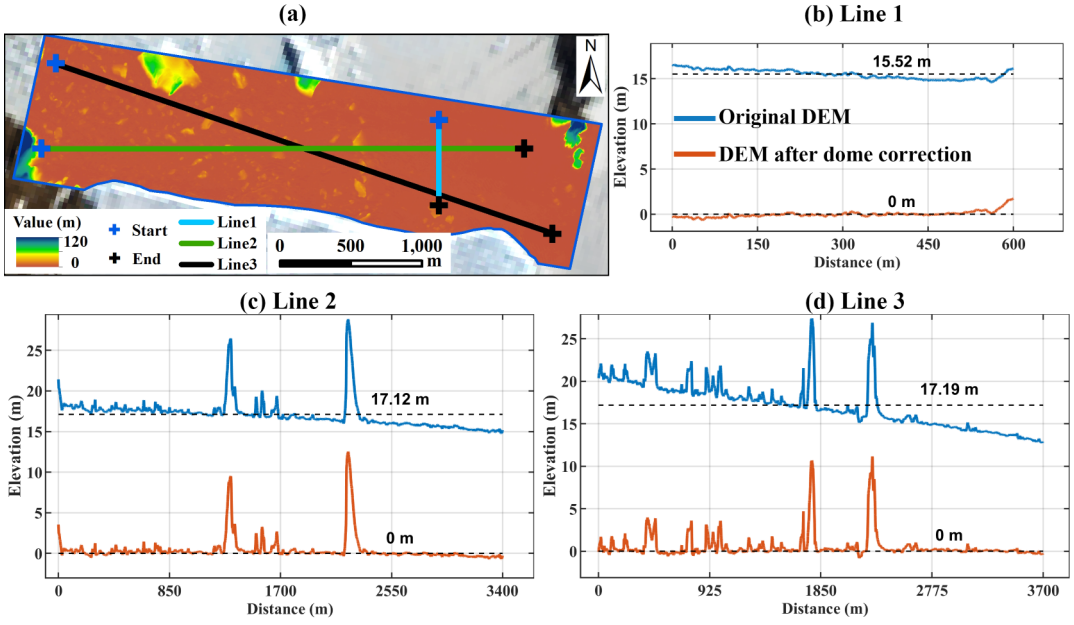

Figure 5. DSM before and after dome effect correction. (a) Selection of cross-sectional lines; (b), (c), and (d) show three cross-sectional profiles, each using the midpoint elevation and 0 m as reference lines.

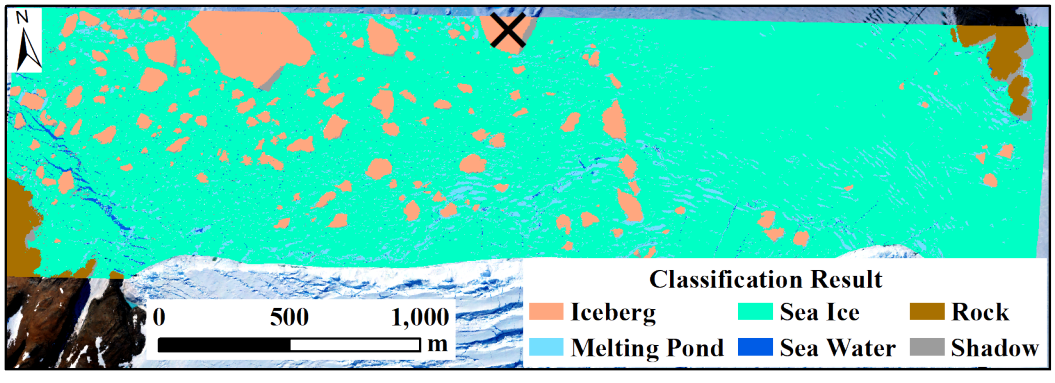

Figure 6. Classification Result. The iceberg, marked as x, was not considered in the subsequent exploration.

is inferred to be caused by the interaction between sea ice, rock, and icebergs, leading to sea ice fracture and exposure of seawater. The classifications further reveal the dynamic changes in the glacial front sea area: icebergs calving from the glacier drift outward under the influence of ocean currents and accumulate near the Larsemann Hills.

https://doi.org/10.5194/egusphere-2025-1884
Preprint. Discussion started: 10 June 2025

Table 3. Confusion Matrix of Classification

Iceberg	Sea Ice	Sea Water	Rock	Melt Pond	Shadow	Total	Producer precision	Kappa
Iceberg	127	3	0	0	0	0	130	0.977
Sea Ice	15	143	1	0	1	0	160	0.894
Sea Water	0	3	81	0	0	3	87	0.931
Rock	0	0	0	50	0	0	50	1.000
Melt Pond	0	0	1	0	46	1	48	0.958
Shadow	0	0	2	0	0	46	48	0.958
Total	142	149	85	50	47	50	523	
User Precision	0.894	0.959	0.953	1.000	0.979	0.920		
Kappa								0.927

A total of 188 icebergs were identified, ranging in equivalent length from 5 m to 300 m, with a total area of 0.384 km^2, a total volume of 0.04 km^3, and a total mass of 3.66×10^7 t. In the range of the UAV image, a particularly large iceberg was also found, with a length of about 420 m and a width of about 300 m, with a maximum and average freeboard of 46.80 m and 21.32 m. This iceberg may further calve into smaller icebergs or move or melt under the action of ocean currents and winds. In addition, the iceberg in the upper part of the image whose basic shape cannot be accurately measured (Fig. 6), and it was not considered in the subsequent size exploration.

4.3 The statistics of icebergs

According to statistics shows in Fig. 7, the maximum and minimum equivalent lengths of these icebergs are 301.52 m and 5.52 m, respectively, with a mean ± standard deviation of 32.72 ± 29.52 m. The maximum and minimum average freeboards of the icebergs are 21.32 m and 0.24 m, respectively, with a mean ± standard deviation of 2.98 ± 2.32 m. The median equivalent length of the icebergs is 27.99 m, and the median average freeboard is 2.56 m. 77.66% of the icebergs in the area had equivalent lengths between 10 m and 60 m, and 90.96% of them had an average freeboard of less than 6 m.

Overall, the freeboard of icebergs shows a positive correlation with their equivalent length (Fig. 7). However, for some icebergs with the same equivalent lengths, the average freeboard varies significantly. For example, an iceberg with an equivalent length of 10 m can have a freeboard difference of 3.5 m, while one with an equivalent length of 85 m may have an average

https://doi.org/10.5194/egusphere-2025-1884
Preprint. Discussion started: 10 June 2025

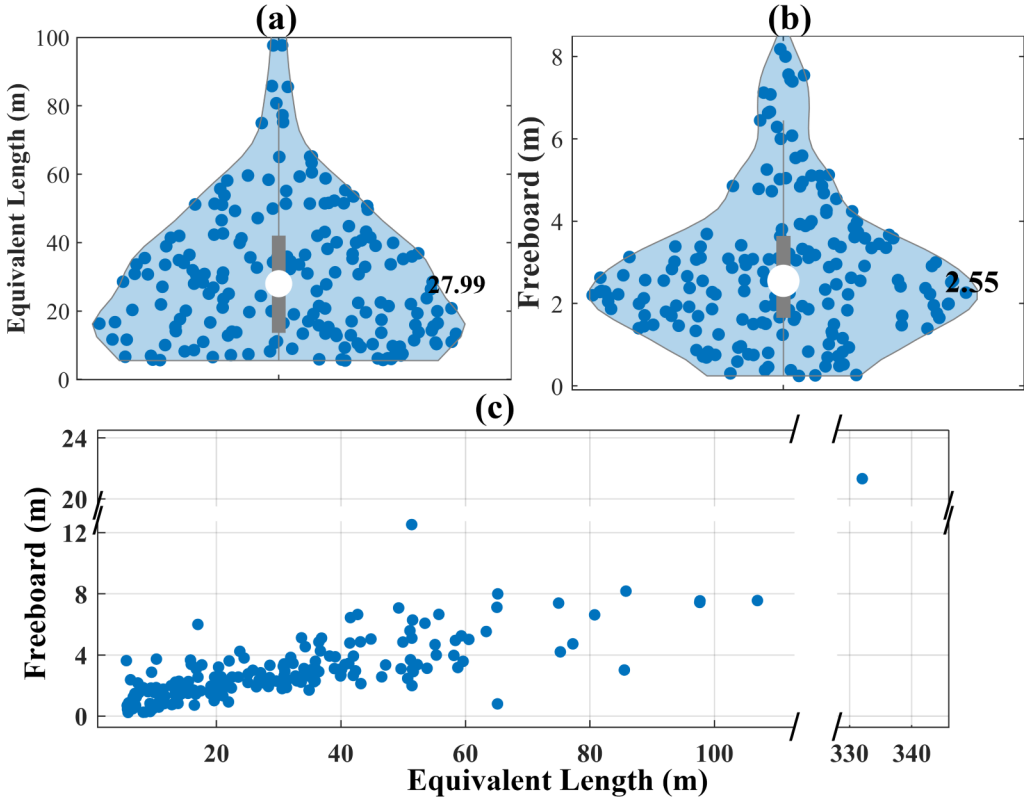

Figure 7. The equivalent length and freeboard of icebergs. (a) and (b) are violin plots of the equivalent length and freeboard, with the median value labeled. (c) The relationship between iceberg equivalent length and freeboard of 187 icebergs in this study, with one iceberg being exceptionally large compared to the others.

freeboard ranging from 3 m to 8 m. This indicates that the iceberg's shape affects the length-freeboard relationship, with shape variations possibly resulting from calving or local conditions like temperature.

Under the drive of the easterly Antarctic Coastal Current (ACC) (Barbara et al., 2010), the icebergs are moved towards the Amery ice shelf on the left, concentrating along the Larsemann Hills on the left side of the area (Fig. 8). Due to their small size, these icebergs are highly susceptible to melting and disappearing due to their surroundings. According to the equivalent length, there are 121 small types of icebergs, and the cross-sectional shapes of these icebergs vary greatly, some are almost square in shape, while others are elongated and rectangular. In terms of average height, 136 icebergs belong to the bergy bit.

The icebergs in the study area follow a power law distribution with a slope of -1.13 (Fig. 9). Compared to the power law distribution with a slope of -1.52 $\pm$ 0.32 for icebergs larger than 0.3 km^2 across the entire Antarctic region (Tournadre et al., 2016), our exponent is closer to 1, indicating that the distribution of iceberg areas is relatively more uniform, with fewer small icebergs in the research area. On one hand, this study monitors icebergs larger than 30 m^2, which are smaller and prone to

https://doi.org/10.5194/egusphere-2025-1884
Preprint. Discussion started: 10 June 2025

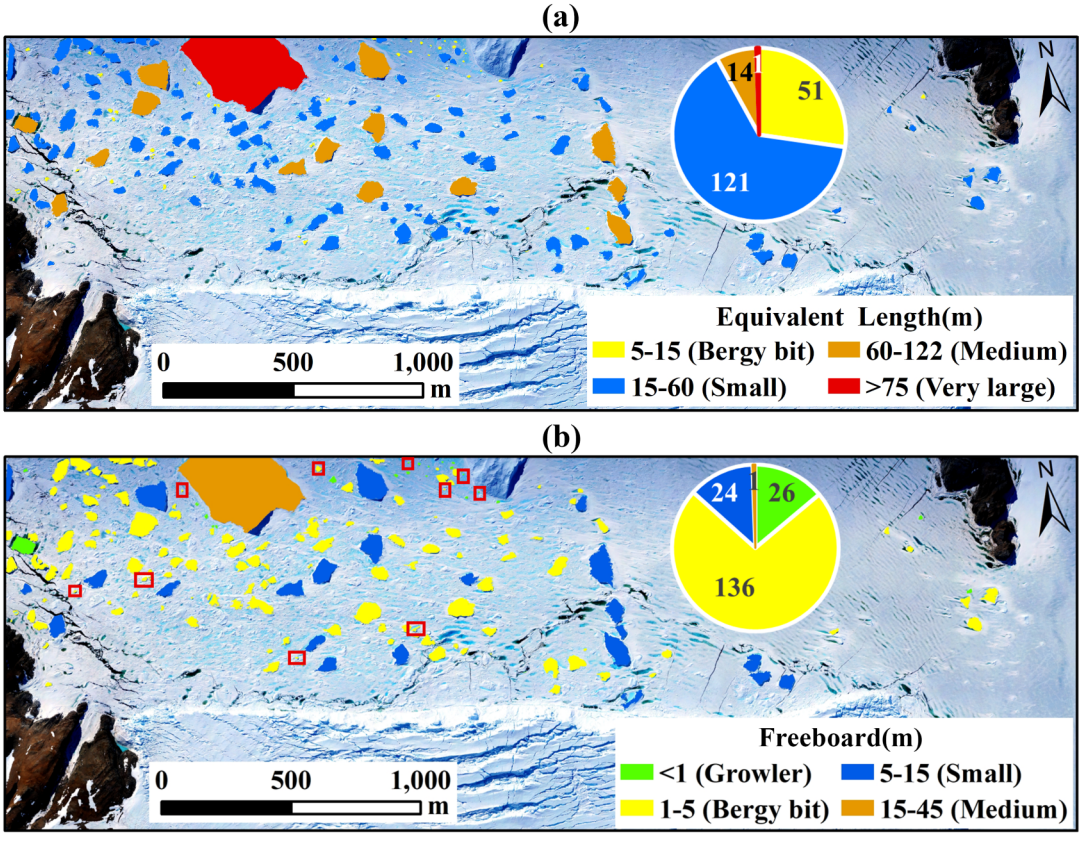

Figure 8. Iceberg types based on two criteria. (a) Based on equivalent length; (b) Based on average freeboard. The red boxes highlight icebergs prone to capsize.

becoming attached to ice ridges, and may be misidentified as sea ice during classification. On the other hand, the abundance of small icebergs is related to the mode of iceberg calving. Whether icebergs undergo secondary calving or only gradually melt affects the number of small icebergs.

4.4 Area/Volume Relationship

By comparing iceberg data obtained from UAV with data from parameterization schemes in ocean models, a clear positive correlation between iceberg area and volume was identified.

In the logarithmic scale, despite the significant difference in magnitude between these two datasets, the fitted lines remain nearly superposed. Notably, in the transition zone between large and small icebergs, ranging from 10^4 to 10^5, two lines are almost perfectly aligned.

https://doi.org/10.5194/egusphere-2025-1884
Preprint. Discussion started: 10 June 2025

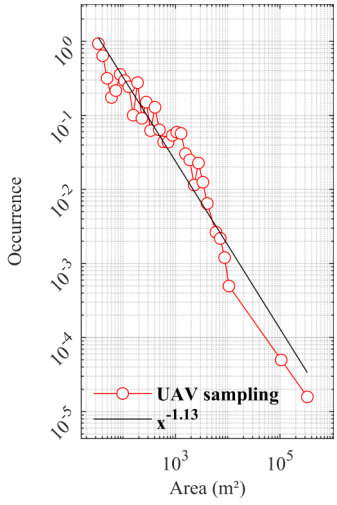

Figure 9. The occurrence distribution of iceberg area in logarithm scale, with power law fitting line.

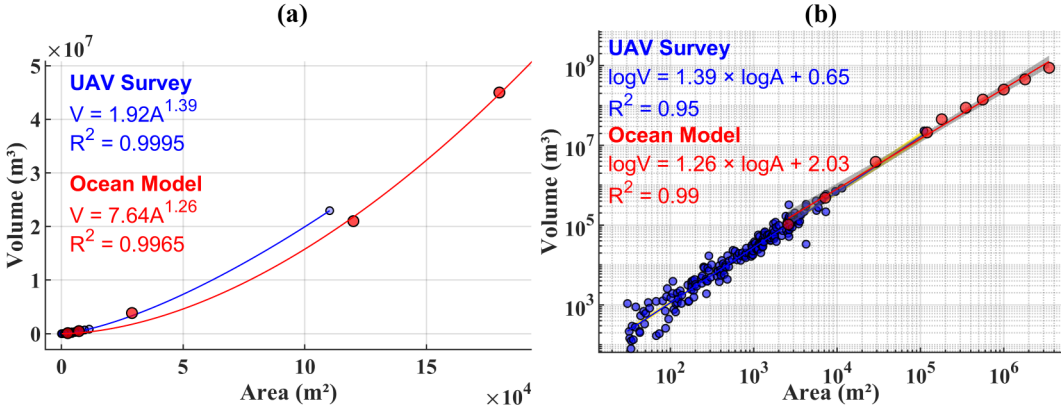

Figure 10. Area/volume power law relationships across two scales. Each point represents an individual iceberg. Blue points indicate data obtained via UAV surveys, with a corresponding blue fitted curve. Red points represent data from the ocean model, accompanied by a red fitted curve. (a) In the linear scale, the model incorporates data from Class 1 to 5(2). (b) In the logarithmic scale (log-log), the model includes data from Class 1 to 10(2); the 95% confidence interval of the UAV survey data is shown as a yellow shaded area, while the gray shaded area represents the corresponding interval for the model.

Based on the capsize formula, more than a dozen relatively small icebergs in the area were identified as having a potential risk of capsizing (indicated by red boxes in Fig. 8(b)). Although these icebergs are not large compared to their relatives in open ocean, their maximum distance from Zhongshan Station is less than 5 km. Under the influence of ocean currents, they may cause collisions between icebergs, posing a potential threat to Zhongshan Station and its surrounding environment.

https://doi.org/10.5194/egusphere-2025-1884
Preprint. Discussion started: 10 June 2025

5 Discussions

5.1 Comparison with iceberg size distribution from other studies

Using satellite remote sensing data, glaciologists can directly measure the area of icebergs and analyze their number and distribution characteristics. Many studies have shown that icebergs follow a power law distribution in area, here we summarize their study areas, source data, iceberg sampling, and fitting power law slope in Table 4.

Table 4. Icebergs' area power law distribution

Study (Year)	Study Area	Data	Iceberg	power law's Slope
This study	Dalk Glacier	UAV DOM & DSM	> 30 m^2	-1.13
Lu et al. (2013)	Xuelong route between 58-68°S	Marine Radar, Sperry Marine	Number: 1085	Ross: -1.448 Weddell: -0.729 Prydz: -0.881
Åström et al. (2014)	Bonavista Bay, Newfoundland	model simulations & camera photos	< 10000 km^2	-2 / 3
Tournadre et al. (2016)	Around Antarctica	Altimeter	0.1 - 10,000 km^2	-1.52 ± 0.32
Kirkham et al. (2017)	Jakobshavn Isbræ,Vaigat	Landsat7 (2013-06-15), Landsat8 (2013-09-16)	10^3 - 10^6 m^2	Jakobshavn Isbræ: -2.4 Vaigat: -2.4
Sulak et al. (2017)	Sermilik, Rink Isbræ, Kangerlussuup Sermia	Landsat8 (2013-2015)	10^3 - 10^6 m^2	Sermilik: -1.95 ± 0.06 Rink Isbræ: -1.87 ± 0.05 Kangerlussuup: -1.62 ± 0.04
Scheick et al. (2019)	Disko Bayc, Sermeq Kujalleq	L7 (2000-2002)& L8 (2013-2015)	>1800 m^2	-1.80 to -2.89
Rezvanbehbahani et al. (2020)	Sermilik, Kangerlussuaq Fjords	PlanetLabs (3m), Sentinel-2 (10m)	>100 m^2	Sermilik: -1.27& -1.29 Kangerlussuaq: -1.24& -1.23

The power law exponent of iceberg area of our UAV data is -1.13. The power law exponent of iceberg area distribution is related to the relative number of different iceberg categories. The variation in this exponent is attributed to the characteristics of calving process of specific glacier and its regional interactions with surrounding ocean environment (Sulak et al., 2017). Our power law slope is smaller than that reported in previous studies, indicating a relatively lower number of small icebergs in the study area. Similar to our findings, in Stern et al. (2016)'s COMPOSITE experiment, the open-ocean iceberg size

https://doi.org/10.5194/egusphere-2025-1884
Preprint. Discussion started: 10 June 2025

distribution exhibits a relatively low abundance of small icebergs — especially those smaller than 10^4 m^2, which deviate from the theoretical -3/2 power law. However, compared to most existing studies, our power law exponent is relatively larger, which requires further analysis.

During iceberg classification, sea ice remains a major factor affecting iceberg extraction, both in open water and within the landfast sea ice regions of our study area. Due to the widespread presence of landfast sea ice, small icebergs are often frozen and immobilized by sea ice, with the resulting surface roughness sometimes confused with sea ice, especially near the glacier front. This may lead to small icebergs being misclassified as sea ice. Changes in calving mechanism significantly impact iceberg size distribution, an increase in calving energy enhances iceberg fragmentation, leading to a higher number of smaller icebergs (Scheick et al., 2019; Åström et al., 2014).

In 2016, Dalk Glacier experienced a major calving event, retreating over 1,000 m and releasing most of its energy. In contrast, the 2019 calving event primarily produced more uniformly sized iceberg blocks. Further analysis of high-resolution imagery is needed to investigate the glacier's calving front and fracture development before and after these events. Additionally, small icebergs in this area may not continue to fragment into smaller pieces but instead gradually shrink and disappear through melting. This hypothesis requires determining the critical size for further fragmentation, alongside multi-temporal high-resolution data to calculate the ice flux of small icebergs and track their melting and potential re-fragmentation processes.

In Greenland's narrow fjords, estimating the total number of icebergs and freshwater flux, and further inferring glacier calving flux, is relatively straightforward, as these regions are largely unaffected by external ocean currents, and icebergs typically originate from calving events of a single glacier. However, our study area, Dalkoybukta Bay in front of Dalk Glacier, is a relatively open coastal region influenced by external ocean currents. Icebergs frequently enter and exit the area, driven by the Antarctic Coastal Current. Therefore, monitoring ice flux based on extracted icebergs require high spatial resolution iceberg drift velocity data, supplemented with high temporal resolution imagery to track dynamic changes of glaciers.

5.2 Scaling analysis in glacier and iceberg geometry

The power law, due to its advantages in quantitatively analyzing complex systems, has been widely applied in physics, biology, and other natural sciences (Pattyn and Huele, 1998). By exploring the relationships between key parameters, it offers indirect solutions to problems that are difficult to observe or solve directly. The theoretical foundation of power laws is well-established and has been extensively validated in glaciology (Bahr et al., 2015). By establishing power law relationships among parameters such as glacier volume, area, thickness, length, response time, and velocity, they enhance understanding of glaciers and expand the application of scaling laws (Bahr et al., 1997). For example, glacier area—easily obtained through remote sensing can be used to indirectly estimate glacier volume, which is difficult to measure directly, which is widely applied in estimating initial ice volume for estimation of Glacier's mass balance (Bahr et al., 1997; Marzeion et al., 2012; Radić et al., 2014). Or to address the challenge of distinguishing between "glaciers" and "ice caps" which often lack clear morphological boundaries (Bahr and Pfeffer, 2016).

These well-established applications of power law scaling in mountain glacier studies provide valuable insights for iceberg research. Given the similar challenges in directly measuring parameters such as thickness or volume from planimetric obser-

https://doi.org/10.5194/egusphere-2025-1884
Preprint. Discussion started: 10 June 2025

vations., particularly for small, drifting ice masses, it is reasonable to explore whether similar power law relationships can be applied to icebergs. While the glaciological context differs—icebergs being afloat and detached rather than grounded — the potential to leverage accessible surface measurements to estimate more elusive properties like volume offers a promising parallel.

In recent iceberg studies, Stuckey et al. (2016) refined the power law relationships between iceberg draft, mass, and waterline length using geometric measurements (e.g., length, width, and sail height) along with three-dimensional iceberg profiles. Their study also updated the iceberg shape database and the Iceberg Load Software (ILS). By simulating generalized structural interactions with ILS, they demonstrated how the updated models, distributions, and scaling relationships affect the estimation of design loads and moments. Furthermore, analysis of Greenland fjord icebergs revealed a clear power law relationship between iceberg area and volume (Sulak et al., 2017). Inspired by the success of area–volume scaling in glacier studies, we further investigate whether nearshore small icebergs exhibit similar power law characteristics, thus extending the study of iceberg geometric relationships from medium or large icebergs to small icebergs. In our study, by comparing the iceberg parameterization data applied in large scale ocean model with our UAV-derived iceberg data, we find that the power law fitting results are quite consistent. This suggests that these widely used parameterization schemes in numerical ocean model align with our research findings on small icebergs, in terms of the size distribution patterns derived from large icebergs observed for large icebergs. It may also provide a new perspective for characterizing icebergs based on power law coefficients.

However, compared to the results of Sulak et al. (2017) and Schild et al. (2021), we observe a different power law coefficient. One possible reason is the significant locational difference between our study area and theirs. Small icebergs are more susceptible to ocean currents during the drifting process, which may lead to enhanced fragmentation and surface melting, thereby altering their geometry and affecting the area/volume relationship. In addition, this study focuses specifically on small icebergs (with area less than 30 m^2), which are underrepresented in some earlier datasets. The limited icebergs' number may also constrain the ability to fit a power law trend across a broader size range. As a result, the scaling coefficient derived here likely reflects the characteristics of the small iceberg population rather than a full-size spectrum.

5.3 Prospects and challenges of UAVs in iceberg research

Existing research has demonstrated that, in Antarctica, direct georeferencing schemes for UAV photogrammetry without GCPs can generate high-accuracy DOMs and DSMs in a reliable and feasible manner (Tang et al., 2024). This allows us to analyze detailed changes (Fig. 11) in surface morphology on finer maps and track changes in polar snow and ice environments (Bhardwaj et al., 2016; Li et al., 2021, 2023). In iceberg extraction using optical imagery, due to data resolution typically exceeding 10 m, icebergs usually need to cover more than five pixels to be accurately identified in the ocean. Therefore, icebergs extracted from satellite remote sensing typically have sizes greater than 50 meters, while UAVs have a clear advantage in monitoring icebergs smaller than 50 meters. Furthermore, in calculating iceberg volume and ice flux, the shape of icebergs is usually inferred based on assumption of certain area/aspect ratio, and volume is then estimated (Dammann et al., 2019). In this research, we directly measured the iceberg area and freeboard height using high-resolution UAV data without relying on thickness-based

https://doi.org/10.5194/egusphere-2025-1884
Preprint. Discussion started: 10 June 2025

shape assumptions, achieving the goal of obtaining iceberg freeboard volume directly from DSM data, thereby more accurately fitting the relationship between area and volume.

The modeling results for the area/volume relationship of icebergs are in good agreement with the trends of existing parameterization models, confirming the feasibility and reliability of UAVs in extracting iceberg geometric shape information. Previous studies have shown that using UAV platforms, combined with cameras, GPS, beacons, and other data collection devices, can overcome the limitations of temporal and spatial resolution during iceberg tracking and sampling, reducing location measurement errors in ocean studies (Carlson and Rysgaard, 2018), and enabling high-frequency tracking of the position, drift speed, and direction of individual icebergs (Jones and Gudmundsson, 2015; McGill et al., 2011), as well as accurate 3D modeling (Carlson et al., 2019). This research explores the relationship between the area and volume of icebergs at a fine scale, from individual icebergs to the whole, with the aim of providing small iceberg samples for parameterization research. Although small icebergs are individually smaller, their large number means they make a significant contribution to the iceberg freshwater flux (Rezvanbehbahani et al., 2020). Future research could further leverage UAV's advantages, combining various data collection methods, to extract more small iceberg samples and build a small iceberg database containing information such as location, length, shape, area, and volume. Additionally, AUVs can be combined to conduct more detailed underwater ice body measurements, obtaining complex picture of iceberg from more angles and further understanding their growth and decay patterns, similar to the research of sea ice (Fan et al., 2023). With the help of rapid profiling systems such as C-CORE's Smart Iceberg Management System (SIMS), it is possible to quickly generate 3D models of iceberg structures, improving both data processing efficiency and modeling accuracy. These high-quality profiles can support the development of iceberg databases and enhance future model training efforts (McGuire et al., 2016).

However, due to the harsh Antarctic environment, it is difficult to evenly distribute control points in polar regions (Li et al., 2019). The sea ice in the front sea area is thin and flat, making it challenging to set control points during the data collection process. The absence of control points and check points may reduce the accuracy of the products (Tang et al., 2024). The preliminary synthesized DSM shows a sea ice thickness of over ten meters in the study area, which diverges markedly from annual monitoring records near Zhongshan Station, where the maximum observed sea ice thickness reached approximately 1.6 m (Zhao et al., 2019). It reveals a pronounced dome effect in the DSM of this area, which will affect the accuracy of iceberg geometric shape extraction and necessitate preprocessing steps. Generally, carefully designing the collection route before the flight or slightly deviating from the vertical flight path during the mission can alleviate the dome effect (James and Robson, 2014).

This research improves the method proposed by Magri and Toldo (2017) for correcting the posterior dome effect in nearly flat terrain, applying it to correct the dome errors in the original DSM of the front sea area of our study region. Specifically, flat sea ice regions are used to capture and reconstruct the defective dome effect, and the dome errors are removed from the original DSM by iteratively reconstructing the geometry of a paraboloid surface. This method takes full advantage of the characteristic of thinner sea ice in the Antarctic summer and has yielded good results in error correction of the DSM. However, although the ice in thin ice regions is very thin, the actual freeboard of sea ice is not necessarily 0 m. As for this research, we are more concerned with the relative values of elevation differences, so the impact is minimal. The relative accuracy (sub-meter level)

https://doi.org/10.5194/egusphere-2025-1884
Preprint. Discussion started: 10 June 2025

without GCP is sufficient for iceberg surveys (Tang et al., 2024; Li et al., 2019). In the future, if conditions allow, further control points can be set on glacier surfaces, icebergs, sea ice, and mountain areas to explore the applicability and accuracy improvement of this method.

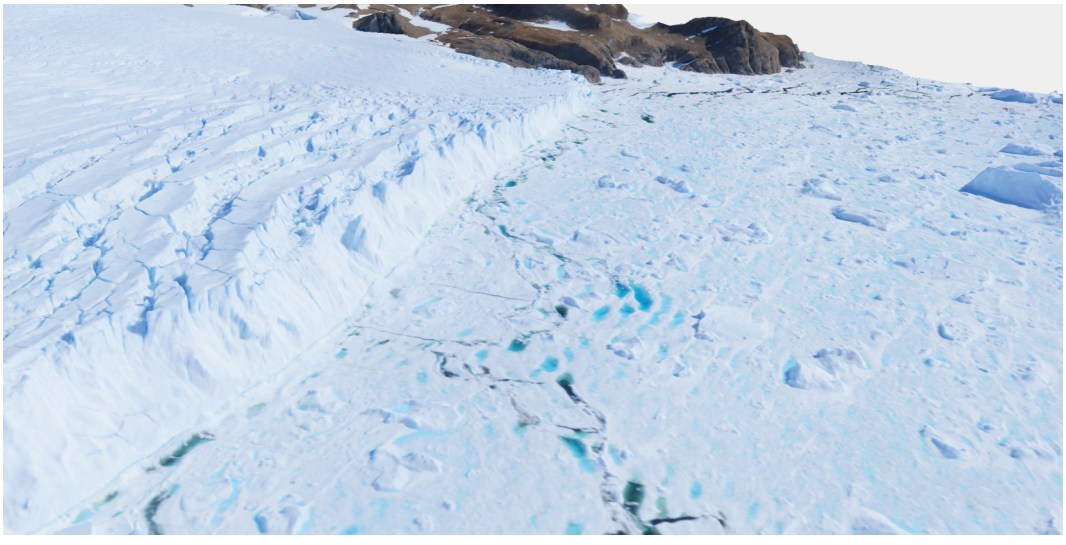

Figure 11. The image shows a 3D map generated using DOM and DSM data acquired by UAV on December 17, 2019. The distribution of icebergs, melt ponds, and other surface features in the nearshore area of Dalk Glacier can be clearly observed.

6 Conclusions

This research is based on high-resolution UAV imagery obtained from the 36th Antarctic Expedition. After performing the photogrammetric process and mitigating the dome effect through paraboloid fitting, we employed superpixel segmentation and random forest classification methods to extract icebergs from the nearshore sea in front of the Dalk Glacier, East Antarctica. The area and freeboard of the icebergs were directly measured, and their volume was calculated from volume above waterline. The results show that the method used to fit the surface effectively removes dome effect from DSM images. A total of 187 icebergs were extracted, with significant variation in equivalent length and freeboard. The area of the icebergs follows a power law distribution with a slope of -1.13. An evident power law relationship between the area and volume of the icebergs was observed, which aligns surprisingly well with the iceberg size distribution parameterization and area/volume scaling relationship from existing ocean model. The geometrical data of the measured icebergs were used to validate the ocean model parameterization scheme based on larger-scale icebergs, and it was found to be applicable to smaller-scale icebergs as well.

This research demonstrates the unique advantages of UAVs in extracting iceberg geometric features, particularly in the fine-scale observation of small icebergs. Through high-resolution DOM and DSMs, we were able to directly measure the freeboard

https://doi.org/10.5194/egusphere-2025-1884
Preprint. Discussion started: 10 June 2025

and volume of the icebergs without relying on empirical aspect ratio assumption, potentially more accurate estimate for iceberg freshwater flux.

Although UAVs show great potential in polar iceberg research, they still face challenges. For example, establishing control points, which is supposed to be a necessary step in UAV surveys over land, often encounters practical difficulties over fragile sea ice in the harsh Antarctic environment. Such absence can lead to systematic errors such as dome effects in DSM generation, which need to be addressed by optimizing flight paths and data processing methods. The relatively small number of small icebergs in the study area is related to the state during their disintegration and the limits of secondary fragmentation of icebergs. This can be a focus for future research that uses UAVs for detailed studies of small icebergs. Further, our study reliance on a single instantaneous sampling may constrain the comprehensive interpretation of iceberg dynamic processes, necessitating supplementary multi-temporal observational data to refine the characterization of iceberg kinematics and morphological evolution patterns. Future studies could further explore the drifting, melting, and secondary fracturing processes of small icebergs using multi-temporal high-resolution data, providing more comprehensive data to support iceberg 3D profiling and dynamic modeling.

Overall, UAV technology offers new tools and methods for polar iceberg research and is expected to play an important role in iceberg monitoring, freshwater flux estimation, and supplementing ocean model parameterization schemes.

Code and data availability. The data and code for eliminating the dome effect, image classification, and area/volume relationship is available at https://doi.org/10.5281/zenodo.15246443. The UAV products and other raw data are available from the authors on request.

Author contributions. MN: Writing original draft, Visualization, Software, Formal analysis, Methodology. XL: Formal analysis, Conceptualization, Methodology, Data collection. TL: Conceptualization, Supervision, Methodology, Review and editing. TZ: Review, Discussion, Data collection. LZ: Review and editing. QL: Review and editing. XC: Review and editing.

Competing interests. The authors declare no conflict of interest related to this work.

Disclaimer. Copernicus Publications remains neutral with regard to jurisdictional claims in published maps and institutional affiliations.

Financial support. This research was supported by the National Natural Science Foundation of China (42206249, 42306263, 42306256, 42422606), the Innovation Group Project of Southern Marine Science and Engineering Guangdong Laboratory (Zhuhai) under Grant (311021008), and the 'Pioneer' and 'Leading Goose' R&D Program of Zhejiang Province (2025C01074).

https://doi.org/10.5194/egusphere-2025-1884
Preprint. Discussion started: 10 June 2025

Acknowledgements. We also greatly thank NASA for providing the Landsat-8 data, the Chinese National Antarctic Research Expedition (CHINARE) for logistical support, and Feima Robotics for technical assistance.

https://doi.org/10.5194/egusphere-2025-1884
Preprint. Discussion started: 10 June 2025

References

Achanta, R., Shaji, A., Smith, K., Lucchi, A., Fua, P., and Süsstrunk, S.: SLIC superpixels compared to state-of-the-art superpixel methods, IEEE Transactions on Pattern Analysis and Machine Intelligence, 34, 2274–2282, https://doi.org/10.1109/TPAMI.2012.120, 2012.

Alley, R. B., Cuffey, K. M., Bassis, J. N., Alley, K. E., Wang, S., Parizek, B. R., Anandakrishnan, S., Christianson, K., and DeConto, R. M.: Iceberg calving; regimes and transitions, Annual review of earth and planetary sciences, 51, 189–216, https://doi.org/10.1146/annurev-earth-032320-110916, 2023.

Bahr, D. B. and Pfeffer, W. T.: Crossover scaling phenomena for glaciers and ice caps, Journal of Glaciology, 62, 299–309, https://doi.org/10.1017/jog.2016.6, 2016.

Bahr, D. B., Meier, M. F., and Peckham, S. D.: The physical basis of glacier volume-area scaling, Journal of Geophysical Research, 102, 20 355–20 362, https://doi.org/10.1029/97JB01696, 1997.

Bahr, D. B., Pfeffer, W. T., and Kaser, G.: A review of volume-area scaling of glaciers, Reviews of Geophysics, 53, 95–140, https://doi.org/10.1002/2014RG000470, 2015.

Barbara, L., Crosta, X., Massé, G., and Ther, O.: Deglacial environments in eastern Prydz Bay, East Antarctica, Quaternary Science Reviews, 29, 2731–2740, https://doi.org/10.1016/j.quascirev.2010.06.027, 2010.

Barbat, M. M., Rackow, T., Hellmer, H. H., Wesche, C., and Mata, M. M.: Three years of near-coastal Antarctic iceberg distribution from a machine learning approach applied to SAR imagery, Journal of Geophysical Research: Oceans, 124, 6658–6672, https://doi.org/10.1029/2019JC015205, 2019.

Benn, D. I., Warren, C. R., and Mottram, R. H.: Calving processes and the dynamics of calving glaciers, Earth-Science Reviews, 82, 143–179, https://doi.org/10.1016/j.earscirev.2007.02.002, 2007.

Bhardwaj, A., Sam, L., Akanksha, Martín-Torres, F. J., and Kumar, R.: UAVs as remote sensing platform in glaciology: Present applications and future prospects, Remote sensing of environment, 175, 196–204, https://doi.org/10.1016/j.rse.2015.12.029, 2016.

Bigg, G. R., Cropper, T. E., O Neill, C. K., Arnold, A. K., Fleming, A. H., Marsh, R., Ivchenko, V., Fournier, N., Osborne, M., and Stephens, R.: A model for assessing iceberg hazard, Natural Hazards, 92, 1113–1136, https://doi.org/10.1007/s11069-018-3243-x, 2018.

Budge, J. S. and Long, D. G.: A comprehensive database for Antarctic iceberg tracking using scatterometer data, IEEE Journal of Selected Topics in Applied Earth Observations and Remote Sensing, 11, 434–442, https://doi.org/10.1109/JSTARS.2017.2784186, 2018.

Carlson, D. F. and Rysgaard, S.: Adapting open-source drone autopilots for real-time iceberg observations, MethodsX, 5, 1059–1072, https://doi.org/10.1016/j.mex.2018.09.003, 2018.

Carlson, D. F., Pasma, J., Jacobsen, M. E., Hansen, M. H., Thomsen, S., Lillethorup, J. P., Tirsgaard, F. S., Flytkjær, A., Melvad, C., Laufer, K., Lund-Hansen, L. C., Meire, L., and Rysgaard, S.: Retrieval of ice samples using the ice drone, Frontiers in Earth Science, 7, 287, https://doi.org/10.3389/feart.2019.00287, 2019.

Chen, Y., Zhou, C., Ai, S., Liang, Q., Zheng, L., Liu, R., and Lei, H.: Dynamics of Dalk Glacier in east Antarctica derived from multisource satellite observations since 2000, Remote sensing, 12, 1809, https://doi.org/10.3390/rs12111809, 2020.

Dammann, D. O., Eriksson, L. E. B., Nghiem, S. V., Pettit, E. C., Kurtz, N. T., Sonntag, J. G., Busche, T. E., Meyer, F. J., and Mahoney, A. R.: Iceberg topography and volume classification using TanDEM-X interferometry, The cryosphere, 13, 1861–1875, https://doi.org/10.5194/tc-13-1861-2019, 2019.

Duprat, L. P. A. M., Bigg, G. R., and Wilton, D. J.: Enhanced Southern Ocean marine productivity due to fertilization by giant icebergs, Nature Geoscience, 9, 219–221, https://doi.org/10.1038/ngeo2633, 2016.

https://doi.org/10.5194/egusphere-2025-1884
Preprint. Discussion started: 10 June 2025

Fan, S., Zhang, X., Zeng, G., and Cheng, X.: Underwater ice adaptive mapping and reconstruction using autonomous underwater vehicles, Frontiers in Marine Science, 10, 1124 752, https://doi.org/10.3389/fmars.2023.1124752, 2023.

Gladstone, R. M., Bigg, G. R., and Nicholls, K. W.: Iceberg trajectory modeling and meltwater injection in the Southern Ocean, Journal of Geophysical Research: Oceans, 106, 19 903–19 915, https://doi.org/10.1029/2000jc000347, 2001.

Guan, Z., Cheng, X., Liu, Y., Li, T., Zhang, B., and Yu, Z.: Effectively extracting iceberg freeboard using bi-temporal Landsat-8 panchromatic image shadows, Remote Sensing, 13, 430, https://doi.org/10.3390/rs13030430, 2021.

Hotzel, I. S. and Miller, J. D.: Icebergs: Their physical dimensions and the presentation and application of measured data, Annals of Glaciology, 4, 116–123, https://doi.org/10.3189/S0260305500005334, 1983.

Ingels, J., Aronson, R. B., Smith, C. R., Baco, A., Bik, H. M., Blake, J. A., Brandt, A., Cape, M., Demaster, D., Dolan, E., et al.: Antarctic ecosystem responses following ice-shelf collapse and iceberg calving: Science review and future research, Wiley Interdisciplinary Reviews: Climate Change, 12, e682, https://doi.org/10.1002/wcc.682, 2021.

James, M. R. and Robson, S.: Mitigating systematic error in topographic models derived from UAV and ground-based image networks, Earth Surface Processes and Landforms, 39, 1413–1420, https://doi.org/10.1002/esp.3609, 2014.

Jones, D. H. and Gudmundsson, G.: Tracking B-31 iceberg with two aircraft-deployed sensors, Natural Hazards and Earth System Sciences, 15, 1243–1250, https://doi.org/10.5194/nhess-15-1243-2015, 2015.

Ke, H., Ai, S., Yan, B., Zhou, C., Wang, Z., Yang, Y., Liu, T., An, J., and Chen, Y.: Iceberg-induced tsunamis near Dålk Glacier, Antarctica, Journal of Surveying Engineering, 148, 04021 027, https://doi.org/10.1061/(ASCE)SU.1943-5428.0000385, 2022.

Kirkham, J. D., Rosser, N. J., Wainwright, J., Vann Jones, E. C., Dunning, S. A., Lane, V. S., Hawthorn, D. E., Strzelecki, M. C., and Szczuciński, W.: Drift-dependent changes in iceberg size-frequency distributions, Scientific reports, 7, 15 991, https://doi.org/10.1038/s41598-017-14863-2, 2017.

Li, T., Shokr, M., Liu, Y., Cheng, X., Li, T., Wang, F., and Hui, F.: Monitoring the tabular icebergs C28A and C28B calved from the Mertz Ice Tongue using radar remote sensing data, Remote Sensing of Environment, 216, 615–625, https://doi.org/10.1016/j.rse.2018.07.028, 2018.

Li, T., Zhang, B., Cheng, X., Westoby, M. J., Li, Z., Ma, C., Hui, F., Shokr, M., Liu, Y., Chen, Z., Zhai, M., and Li, X.: Resolving fine-scale surface features on polar sea ice: A first assessment of UAS photogrammetry Without ground control, Remote Sensing, 11, 784, https://doi.org/10.3390/rs11070784, 2019.

Li, T., Liu, Y., and Cheng, X.: Recent and imminent calving events do little to impair Amery ice shelf's stability, Acta Oceanologica Sinica= Hai Yang Hsueh Pao, 39, 168–170, https://doi.org/10.1007/s13131-020-1600-6, 2020a.

Li, T., Zhang, B., Xiao, W., Cheng, X., Li, Z., and Zhao, J.: UAV-based photogrammetry and LiDAR for the characterization of ice morphology evolution, IEEE Journal of Selected Topics in Applied Earth Observations and Remote Sensing, 13, 4188–4199, https://doi.org/10.1109/JSTARS.2020.3010069, 2020b.

Li, T., Zhang, B., Cheng, X., Hui, F., and Li, Y.: Leveraging the UAV to support Chinese Antarctic expeditions: A new perspective, Advances in Polar Science, 32, 67–74, https://doi.org/10.13679/j.advps.2020.0018, 2021.

Li, Y., Qiao, G., Popov, S., Cui, X., Florinsky, I. V., Yuan, X., and Wang, L.: Unmanned aerial vehicle remote sensing for Antarctic research: A review of progress, current applications, and future use cases, IEEE Geoscience and Remote Sensing Magazine, 11, 73–93, https://doi.org/10.1109/MGRS.2022.3227056, 2023.

Liu, X., Cheng, X., Liang, Q., Li, T., Peng, F., Chi, Z., and He, J.: Grounding event of iceberg D28 and its interactions with seabed topography, Remote Sensing, 14, 154, https://doi.org/10.3390/rs14010154, 2022.

https://doi.org/10.5194/egusphere-2025-1884
Preprint. Discussion started: 10 June 2025

Lu, P., Li, Z., Shi, L., and Huang, W.: Marine radar observations of iceberg distribution in the summer Southern Ocean, Annals of Glaciology, 54, 35–40, https://doi.org/10.3189/2013AoG62A086, 2013.

Magri, L. and Toldo, R.: Bending the doming effect in structure from motion reconstructions through bundle adjustment, The International Archives of the Photogrammetry, Remote Sensing and Spatial Information Sciences, XLII-2/W6, 235–241, https://doi.org/10.5194/isprs-archives-XLII-2-W6-235-2017, 2017.

Marzeion, B., Jarosch, A. H., and Hofer, M.: Past and future sea-level change from the surface mass balance of glaciers, The Cryosphere, 6, 1295–1322, https://doi.org/10.5194/tc-6-1295-2012, 2012.

McGill, P. R., Reisenbichler, K. R., Etchemendy, S. A., Dawe, T. C., and Hobson, B. W.: Aerial surveys and tagging of free-drifting icebergs using an unmanned aerial vehicle (UAV), Deep Sea Research Part II: Topical Studies in Oceanography, 58, 1318–1326, https://doi.org/10.1016/j.dsr2.2010.11.007, 2011.

McGuire, P., Younan, A., Wang, Y., Bruce, J., Gandi, M., King, T., Keeping, K., and Regular, K.: Smart iceberg management system – Rapid Iceberg Profiling system, in: OTC Arctic Technology Conference, vol. 16OARC, pp. OTC–27 473–MS, https://doi.org/10.4043/27473-MS, 2016.

Mishra, P., Tripathi, N., Singh, S. K., Oza, S. R., Solanki, P. M., and Bhatt, N. Y.: Comprehending the surface melt characteristics, calving processes, and seasonal ice velocity of Dålk glacier in Larsemann Hills, East Antarctica, Polar Science, 42, 101 081, https://doi.org/10.1016/j.polar.2024.101081, 2024.

Moctezuma-Flores, M., Parmiggiani, F., and Guerrieri, L.: Tracking of the huge Antarctic iceberg A-76, Remote sensing letters, 14, 10–20, https://doi.org/10.1080/2150704X.2022.2152292, 2023.

Orheim, O.: Physical characteristics and life expectancy of tabular Antarctic icebergs, Annals of Glaciology, 1, 11–18, https://doi.org/10.3189/S0260305500016888, 1980.

Pattyn, F. and Huele, W. V.: Power law or power flaw, Earth Surface Processes and Landforms, 23, 761–767, https://api.semanticscholar.org/CorpusID:55454457, 1998.

Qiao, G., Yuan, X., Florinsky, I., Popov, S., He, Y., and Li, H.: Topography reconstruction and evolution analysis of outlet glacier using data from unmanned aerial vehicles in Antarctica, International Journal of Applied Earth Observation and Geoinformation, 117, 103 186, https://doi.org/10.1016/j.jag.2023.103186, 2023.

Radić, V., Bliss, A., Beedlow, A. C., Hock, R., Miles, E., and Cogley, J. G.: Regional and global projections of twenty-first century glacier mass changes in response to climate scenarios from global climate models, Climate Dynamics, 42, 37–58, https://doi.org/10.1007/s00382-013-1719-7, 2014.

Rezvanbehbahani, S., Stearns, L. A., Keramati, R., Shankar, S., and van der Veen, C. J.: Significant contribution of small icebergs to the freshwater budget in Greenland fjords, Communications Earth and Environment, 1, https://doi.org/10.1038/s43247-020-00032-3, 2020.

Scheick, J., Eederlin, E. M., and Hamilton, G.: Semi-automated open water iceberg detection from Landsat applied to Disko Bay, West Greenland, Journal of Glaciology, 65, 468–480, https://doi.org/10.1017/jog.2019.23, 2019.

Schild, K. M., Sutherland, D. A., Elosegui, P., and Duncan, D.: Measurements of iceberg melt rates using high-resolution GPS and iceberg surface scans, Geophysical Research Letters, 48, e2020GL089 765, https://doi.org/10.1029/2020GL089765, 2021.

Skrypitsyna, T. N., Florinsky, I. V., and Qiao, G.: Motion of the Dålk Glacier (Prydz Bay, East Antarctica): Application of unmanned aerial survey, Polar Science, 38, 100 949, https://doi.org/10.1016/j.polar.2023.100949, 2023.

Stern, A. A., Adcroft, A., and Sergienko, O.: The effects of Antarctic iceberg calving-size distribution in a global climate model, Journal of Geophysical Research: Oceans, 121, 5773–5788, https://doi.org/10.1002/2016JC011835, 2016.

https://doi.org/10.5194/egusphere-2025-1884
Preprint. Discussion started: 10 June 2025

Stuart, K. M. and Long, D. G.: Tracking large tabular icebergs using the SeaWinds Ku-band microwave scatterometer, Deep Sea Research Part II: Topical Studies in Oceanography, 58, 1285–1300, https://doi.org/10.1016/j.dsr2.2010.11.004, 2011.

Stuckey, P., Younan, A., Parr, G., Fuglem, M., and Habib, K.: Updating the iceberg load software using high resolution iceberg profiles, in: OTC Arctic Technology Conference, vol. 16OARC, pp. OTC–27 492–MS, https://doi.org/10.4043/27492-MS, 2016.

Sulak, D. J., Sutherland, D. A., Enderlin, E. M., Stearns, L. A., and Hamilton, G. S.: Iceberg properties and distributions in three Greenlandic fjords using satellite imagery, Annals of Glaciology, 58, 92–106, https://doi.org/10.1017/aog.2017.5, 2017.

Tang, L., Qiao, G., Li, B., Yuan, X., Ge, H., and Popov, S.: GNSS-supported direct georeferencing for UAV photogrammetry without GCP in Antarctica: A case study in Larsemann Hills, Marine Geodesy, 47, 324–351, https://doi.org/10.1080/01490419.2024.2316089, 2024.

Tournadre, J., Bouhier, N., Girard Ardhuin, F., and Rémy, F.: Antarctic icebergs distributions 1992–2014, Journal of Geophysical Research: Oceans, 121, 327–349, https://doi.org/10.1002/2015JC011178, 2016.

Wackrow, R. and Chandler, J. H.: Minimising systematic error surfaces in digital elevation models using oblique convergent imagery, The Photogrammetric Record, 26, 16–31, https://doi.org/10.1111/j.1477-9730.2011.00623.x, 2011.

Wadhams, P. and Krogh, B.: Operational history and development plans for the use of AUVs and UAVs to map sea ice topography, Polar Science, 21, 195–203, https://doi.org/10.1016/j.polar.2019.07.004, 2019.

Weeks, W. F. and Mellor, M.: SOME ELEMENTS OF ICEBERG TECHNOLOGY, in: Iceberg Utilization, edited by Husseiny, A., pp. 45–98, Pergamon, ISBN 978-0-08-022916-4, https://doi.org/10.1016/B978-0-08-022916-4.50015-7, 1978.

Yurtseven, H.: Comparison of GNSS-, TLS- and different altitude UAV-generated datasets on the basis of spatial differences, ISPRS International Journal of Geo-Information, 8, 175, https://doi.org/10.3390/ijgi8040175, 2019.

Zhao, J., Yang, Q., Cheng, B., Leppäranta, M., Hui, F., Xie, S., Chen, M., Yu, Y., Tian, Z., Li, M., and Zhang, L.: Spatial and temporal evolution of landfast ice near Zhongshan Station, East Antarctica, over an annual cycle in 2011/2012, Acta Oceanologica Sinica, 38, 51–61, https://doi.org/10.1007/s13131-018-1339-5, 2019.

Åström, J. A., Vallot, D., Schäfer, M., Welty, E. Z., O Neel, S., Bartholomaus, T. C., Liu, Y., Riikilä, T. I., Zwinger, T., Timonen, J., and Moore, J. C.: Termini of calving glaciers as self-organized critical systems, Nature Geoscience, 7, 874–878, https://doi.org/10.1038/ngeo2290, 2014.